Estimating Cloud Optical Depth from Surface Radiometric Observations: Sensitivity to Instrument Noise and Aerosol Contamination

ALAIN BEAULNE

Canadian Meteorological Centre, Meteorological Service of Canada, Dorval, Québec, Canada

HOWARD W. BARKER

Meteorological Service of Canada, Downsview, Ontario, Canada

JEAN-PIERRE BLANCHET

Université du Québec à Montréal, Montréal, Québec, Canada

(Manuscript received 21 October 2003, in final form 30 January 2005)

ABSTRACT

The spectral-difference algorithm of Barker and Marshak for inferring optical depth τ of broken clouds has been shown numerically to be potentially useful. Their method estimates cloud-base reflectance and τ using spectral radiometric measurements made at the surface at two judiciously chosen wavelengths. Here it is subject to sensitivity tests that address the impacts of two ubiquitous sources of potential error: instrument noise and presence of aerosol. Experiments are conducted using a Monte Carlo photon transport model, cloud-resolving model data, and surface albedo data from satellite observations. The objective is to analyze the consistency between inherent and retrieved values of τ. Increasing instrument noise, especially if uncorrelated at both wavelengths, decreases retrieved cloud fraction and increases retrieved mean τ. As with all methods that seek to infer τ using passive radiometry, the presence of aerosol requires that threshold values be set in order to discriminate between cloudy and cloud-free columns. A technique for estimating thresholds for cloudy columns is discussed and demonstrated. Finally, it was found that surface type and mean inherent τ play major roles in defining retrieval accuracy.

1. Introduction

The character of the earth's climate is greatly determined by its attempt to balance absorption of incoming solar radiation with outgoing emitted infrared radiation. Clouds attenuate solar radiation and thus play a crucial role in establishing this balance. The extent to which clouds attenuate solar radiation is related directly to their optical depth τ, or vertically integrated extinction. Hence, it is vital that global climate models reproduce correctly the spatial and temporal variations of τ.

Cloud optical depth information is generally retrieved two ways, both of which rely on 1D radiative transfer models. The first uses ground-based observations of downwelling fluxes (spectral or broadband) that are then related to cloud transmittances, and finally to τ (e.g., Leontyeva and Stamnes 1994; Leontieva et al. 1994; Boers 1997; Barker et al. 1998; Boers et al. 2000). The other uses spaceborne (satellite) observations of upwelling radiances that are related to cloud reflectances, and again to τ (e.g., Rossow and Schiffer 1991; Barker and Liu 1995; Loeb and Davies 1996; Loeb and Coakley 1998). These studies are limited, however, by their complete reliance on 1D transfer theory.

Recently, Marshak et al. (2000) proposed a ground-based methodology that relies on disparate optical properties of cloud water droplets and green vegetation at two narrow spectral bands in the visible and near infrared. Using a Monte Carlo radiative transfer algorithm and broken cloud fields derived from Landsat imagery, Barker and Marshak (2001, hereafter BM01)

Corresponding author address: Alain Beaulne, Canadian Meteorological Centre, Meteorological Service of Canada, 2121 Trans-Canada Highway, Dorval, PQ H9J 1J3, Canada.
E-mail: alain.beaulne@ec.gc.ca

demonstrated the potential value of this method for retrieving τ for a wide range of cloud conditions. This was extended to aircraft-mounted radiometers by Barker et al. (2002). While their method does not account for 3D radiative effects, it has demonstrated some ability to retrieve τ for broken clouds.

The purpose of the present study is to numerically assess the sensitivity of BM01's retrieval algorithm to instrument noise and aerosol. Section 2 presents the fundamentals behind the retrieval algorithm and section 3 describes input data and tools used here. Section 4 presents results of the retrievals for different numerical tests, while section 5 finishes with a discussion and conclusion.

2. Cloud optical depth retrieval algorithm

Throughout this paper, all radiometric quantities are normalized by downwelling spectral solar irradiance at the top of the atmosphere. The algorithm formulated by BM01 estimates local cloud-base reflectance into nadir as

$$\rho_\tau = \frac{I_2^\downarrow - I_1^\downarrow}{\alpha_2 \tilde{F}_2^\downarrow - \alpha_1 \tilde{F}_1^\downarrow}, \tag{1}$$

where α_λ, $I_\lambda^\downarrow$, and $\tilde{F}_\lambda^\downarrow$ are respectively local effective surface albedo, downwelling surface radiance, and effective downwelling surface irradiance at wavelengths λ_1 and λ_2. Values of λ_1 and λ_2 should be chosen so that cloud droplet optical properties are very similar but surface albedos are quite different. Thus, the difference in the numerator of (1) eliminates photons that have interacted with clouds only and leaves contributions from photons that have undergone one or more encounters with the surface. In the denominator of (1), $\alpha_\lambda \tilde{F}_\lambda^\downarrow$ can be thought of as upwelling flux at the zenith point on cloud base. Hence, $\tilde{F}_\lambda^\downarrow$ takes into account local cloud structure in the form of an effective averaged downward flux. In its discretized form, with reference to Fig. 1, $\tilde{F}_\lambda^\downarrow$ is approximated as

$$\tilde{F}_\lambda^\downarrow(j) = \frac{\sum_{k=j-n}^{j+n} F_\lambda^\downarrow(k) \cos^3\theta_{j,k}}{\sum_{k=j-n}^{j+n} \cos^3\theta_{j,k}}, \tag{2}$$

where j corresponds to the surface pixel located under the cloud column where τ is sought, k is another surface pixel, $F_\lambda^\downarrow(k)$ is surface irradiance at k, and $\theta_{j,k}$ is the angle between the two segments starting at cloud base over j and joining surface pixel j and k. The cosine term is a weighting factor associated with the relative contribution from pixel k to cloud-base flux at point j. The index n is chosen so that $-80° < \theta_{j,k} < 80°$; contributions from larger angles are negligeable (see BM01, their Fig. 3). Finally, effective local surface albedo α_λ, which should normally rely on the same weighting rule as in (2), will be approximated for simplicity by the pointwise albedo at pixel j. This avoids the difficulty of precise specification of spectral albedos over wide areas. Note that Barker et al.'s (2002) aircraft-based method avoids this complication.

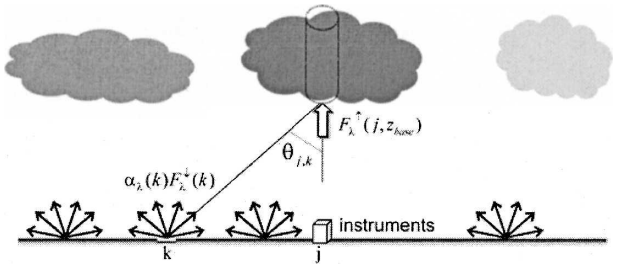

FIG. 1. Determination of cloud-base upward spectral irradiance.

Practically speaking, observed downwelling fluxes needed for estimation of upwelling flux at cloud base are measured as a time series while clouds advect and evolve past the radiometers. Within the frozen turbulence approximation, this is equivalent to taking, in the spatial frame of reference, a 1D transect at the surface as representative of the complete 2D flux field. In the simulations performed here, the cloud field is fixed and values of $F_\lambda^\downarrow(k)$ are obtained from neighboring pixels.

Finally, once cloud-base reflectance is computed, τ is retrieved using a 1D solution of the radiative transfer equation. Exact solutions were computed for 14 values of τ using the 16-stream version of the discrete ordinate method radiative transfer code (DISORT; Stamnes et al. 1988) with Henyey–Greenstein phase function (Henyey and Greenstein 1941) at asymmetry parameter $g = 0.85$ and single-scattering albedo $\varpi_0 = 1$. These data were then fit with a Padé approximant that inflicts an error of about $\pm 0.5\%$ on retrieved values of τ between 0.01 and 100. If retrieved optical depth τ_{ret} exceeds 100, it is reset to 100. If $\tau_{\text{ret}} < 0.01$, it is assumed to be zero. This way, individual observations can be labeled clear or cloudy, thereby enabling estimation of retrieved cloud fraction.

BM01 used two marine boundary layer cloud fields with τ inferred from Landsat imagery (mean inherent optical depth $\bar{\tau}_{\text{inh}} \cong 3$), a Henyey–Greenstein phase function, and homogeneous Lambertian surfaces meant to mimic green vegetation. Spectral wavelengths were assumed to be $\lambda_1 \approx 0.65\mu$m and $\lambda_2 \approx 0.85\mu$m, which for green vegetated surfaces have albedos of $\alpha_1 \approx 0.1$ and $\alpha_2 \approx 0.5$ (Marshak et al. 2000), but corresponding cloud properties are almost identical with $g \approx 0.85$ and $\varpi_0 \approx 1$.

TABLE 1. Cloud field characteristics.

Cloud field	Grid spacing (m)	Domain size (km)	Cloud fraction*	Mean cloud optical depth*
Scattered arctic stratocumulus (A)	25	100.0 × 1.1	0.53	4.3
Broken arctic stratocumulus (B)	25	50.0 × 1.5	0.88	13.9
Fair weather cumulus (C)	50	50.0 × 1.0	0.59	55.8

* These are for columns with $\tau \geq 0.01$.

Results obtained from their simulations were very promising: relative mean bias errors for τ_{ret} were typically <5% and relative variances were almost independent of $\bar{\tau}_{inh}$ and <50%. Frequency distributions and power spectra for τ_{inh} and τ_{ret} were often in excellent agreement. These promising results were the prime motivations for the present study.

3. Methodology

The first step in this evaluation was to simulate cloud fields and radiometric measurements needed by the retrieval algorithm. The second step was to estimate τ_{ret}. For each pixel, τ_{ret} was compared to its inherent counterpart τ_{inh}. Modifications of simulation properties allowed assessment of the algorithm's sensitivity to parameters.

a. Cloud fields

Three 2D cloud fields were used here. All of them vary in the vertical and one horizontal direction while the second horizontal dimension is homogenous. Their domain size is 100 km in the variable horizontal direction and ~2 km in the vertical. They possess periodic horizontal boundaries conditions, and cloud droplet size distributions that are resolved into 1-μm bins between 0 and 20 μm and that vary in space. These fields were generated initially for the Synergy of Passive and Active Instruments (SYPAI) simulator project (Park et al. 2000),and were produced using a variant (Szyrmer 1998; Szyrmer and Zawadzki 1999) of the Canadian Regional Climate Model (Caya and Laprise 1999) with a 2-s time step and 25- to 50-m grid spacing. Cloud microphysics were treated with the method proposed by Brenguier (1991) and applied by Brenguier and Grabowski (1993).

The three cloud fields represent scattered arctic stratocumulus (scene A), broken arctic stratocumulus (scene B), and fair-weather cumulus (scene C). Table 1 gives information about the fields while Fig. 2 shows vertical cross sections of the extinction coefficient for representative segments. Figure 3 presents histograms of τ_{inh} for the three scenes.

b. Surface types

Five types of vegetated ground surfaces were used to underlay the CRCM data: green vegetation, urban, cropland, needleleaf, and broadleaf forest. The green vegetation surface is as in BM01. For the other surfaces, the *Land Cover Map of Canada v1.1* (Cihlar et al. 1999) was used to obtain appropriate surface vegetation distributions (1995 growing season) while the Canada-wide 1-km AVHRR Composite Maps based on Geocoding and Compositing (GEOCOMP) data enhanced with ABC3v2 Software database (available online at http://geogratis.cgdi.gc.ca/) was used to assign typical visible and near-infrared albedos. Table 2 lists values of α_1 and α_2 in addition to $\Delta\alpha_\lambda$ for each of them.

c. Monte Carlo radiative transfer scheme

The Monte Carlo radiative transfer scheme employed in this study was developed originally by Barker (1991). It simulates photon transport for a 3D array of cells and uses random numbers to determine the outcome of events based on probability distributions. Radiometric quantities are computed for all surfaces simultaneously in a single simulation. This approach banks on wavelength invariant droplet phase functions and surface bidirectional reflectance distribution functions.

Each atmospheric cell requires extinction coefficient, g, and ϖ_0 for each atmospheric constituent present. Rayleigh scattering is neglected as wavelengths were longer than 0.65 μm. Radiances were computed using the local estimation method (Marchuk et al. 1980; Marshak et al. 1995). For these simulations, 10^5 photons per column were used.

4. Results

Figure 4 presents an intercomparison plot between inherent and retrieved τ for each cloudy column of the three cloud fields using the green vegetation surface. Two important features are noteworthy. First, retrieved values of τ are very accurate in general and show low variability. Second, there is a tendency for τ to be overestimated for low values and underestimated for higher

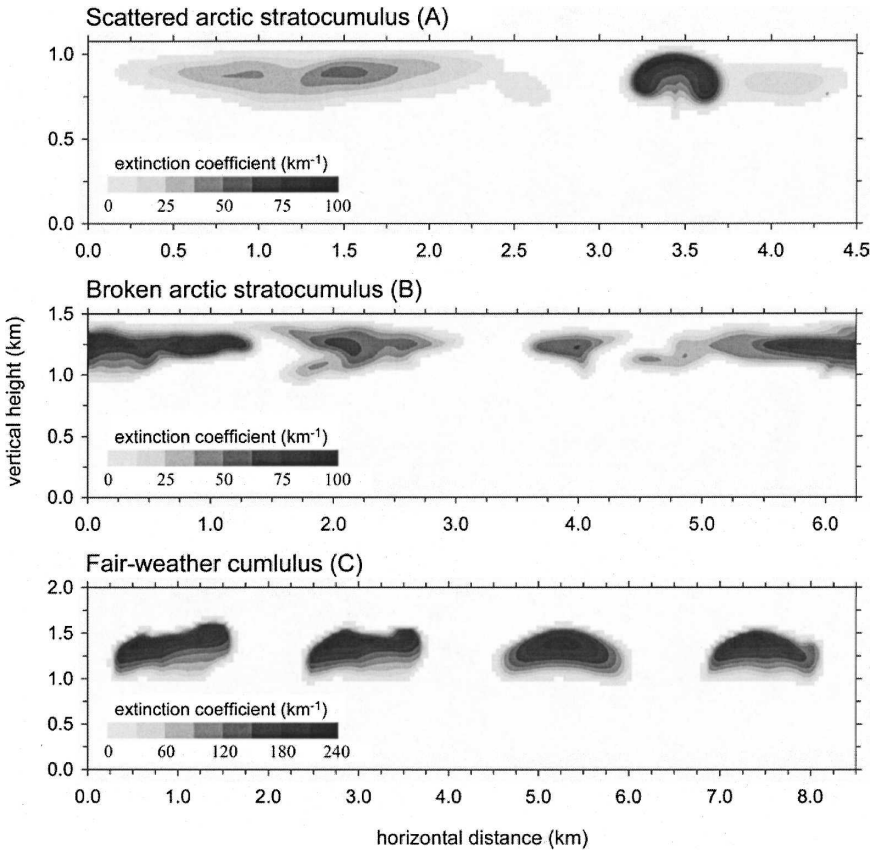

FIG. 2. Cross sections of cloud extinction coefficient (km^{-1}) for representative segments of the three cloud fields used in this study.

values. A similar feature was observed by BM01 and explained by horizontal transport of photons from relatively dense cloud regions to relatively tenuous regions.

Table 3 lists errors made on retrieved average cloud-base reflectance $\overline{\rho}_{\text{ret}}$ that corroborates the findings of the last plot. It also lists errors made on the retrieved average optical depth $\overline{\tau}_{\text{ret}}$. Note the ratio of relative errors in τ to those in ρ as $\overline{\tau}_{\text{inh}}$ increases: 1:1 for scene A, almost 2:1 for B, and nearly 5:1 for C. This shows that a large part of the error made on $\overline{\tau}_{\text{ret}}$ is not due to the retrieval algorithm directly but rather to the increasingly sensitive nonlinear functional relationship between τ and ρ. As clouds thicken and become more reflective, variations in optical depth become increasingly sensitive to variations in reflectance. This is because thicker clouds also transmit less radiation to begin with, so variations of $I_2^{\downarrow} - I_1^{\downarrow}$ do not decrease much as optical depth increases.

a. Sensitivity to instrument noise

In the last analysis, radiometric quantities simulated by the Monte Carlo radiation scheme were used directly in the retrieval algorithm. This is tantamount to the assumption that measurements are almost perfect (not withstanding minor Monte Carlo noise). Though full portrayal of sensor errors is beyond the scope of this study, simulated downwelling surface radiance measurements were contaminated by adding independent random Gaussian noise at both wavelengths. Retrievals were then made using radiance fields altered by noise ranging from 1%–10% at the 95% confidence level. Downwelling surface irradiances were not subject to random noise. This is because effective downwelling irradiances are summations of numerous measured irradiances, and so random errors in the denominator of (1) will be negligible.

Figure 5 illustrates how potentially sensitive retrievals can be to radiance noise. It shows the relative difference between the two downward radiances when they are perfect (as given by the Monte Carlo model) as a function of τ_{inh} for green vegetation, cropland, and coniferous surfaces for cloud field A. Even at $\tau_{\text{inh}} \approx 5$, differences are only about 3%–10%. In practice, these differences should be large compared to measurement

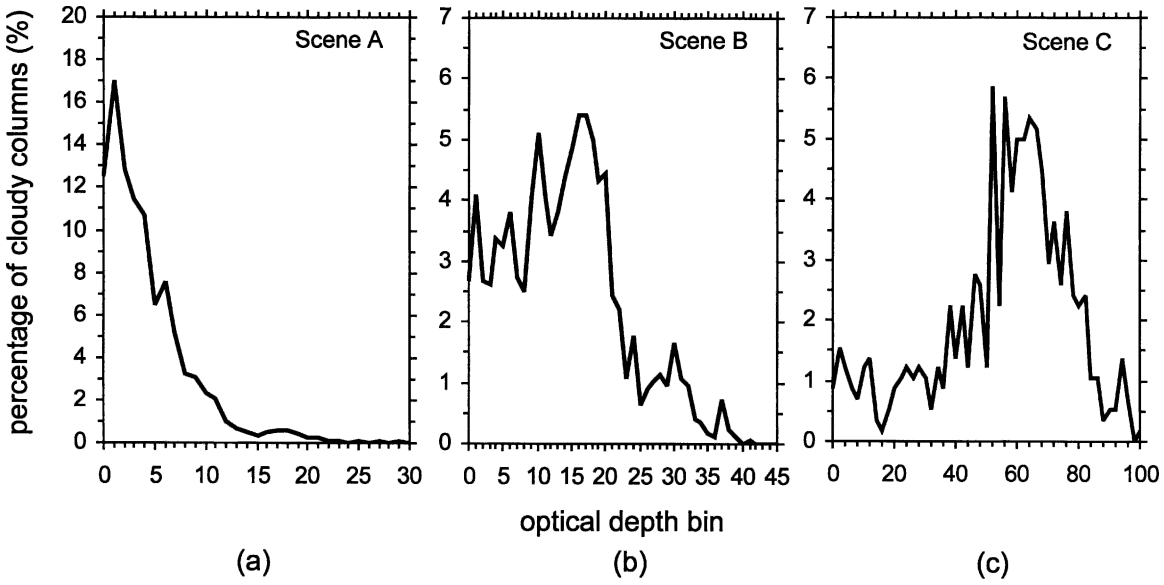

FIG. 3. Percentage of cloudy columns per optical depth bin for the three cloud scenes. Bins widths are 1 for scenes A and B and 2 for scene C.

noise. Retrieval statistics are presented in Fig. 6 where retrieved cloud fraction, $\bar{\tau}_{\text{ret}}$, and root-mean-square error (rmse) are analyzed as a function of radiance noise for the different cloud fields and surface types. Results represent averages over ten independent experiments. The general conclusion is that with increased radiance noise, one can expect retrieved cloud fraction to decrease while $\bar{\tau}_{\text{ret}}$ and its rmse increase.

First, consider the retrieved cloud fraction, which decreases with increasing radiance noise, but whose sensitivity to noise increases as $\Delta\alpha_\lambda$ decreases. If independent random noise added to spectral radiances acts to reduce $\Delta I_\lambda^\downarrow$, radiances can become indistinguishable and even reverse order. In either case, the column is retrieved as cloudless. Noise that is correlated to some extent between the two radiance measurements or uncorrelated leading to a negative measurement error for $I_2^\downarrow$ and positive for $I_1^\downarrow$ might lead to a false clear sky. The latter possibility is the one that has the greater probability to yielding a false cloudless column. As noise increases, large values of τ are more susceptible to this misinterpretation. Surfaces with small $\Delta\alpha_\lambda$ (and thus small $\Delta I_\lambda^\downarrow$ to begin with) are affected most. Estimated cloud fraction for cloud field C is affected weakly by radiance noise since it contains very few small τ.

Turning attention to mean retrieved τ, Fig. 6 shows that it increases with noise amplitude. The misinterpretation related to cloud fraction, as explained above, affects thin columns most and cannot explain fully these

TABLE 2. Surface data characteristics.

Surface type	α_1	α_2	$\Delta\alpha_\lambda$
Green vegetation	0.10	0.50	0.40
Broadleaf	0.05	0.38	0.33
Cropland	0.08	0.37	0.29
Urban	0.10	0.29	0.19
Coniferous	0.04	0.17	0.13

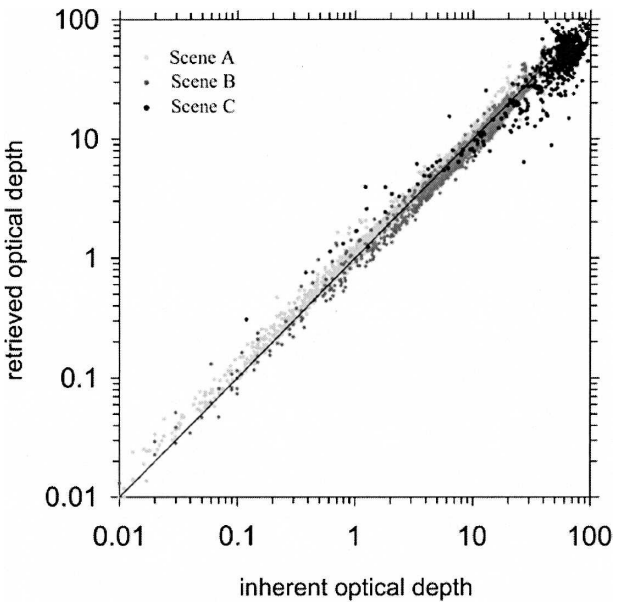

FIG. 4. Scatterplot of retrieved vs inherent optical depth for the cloudy columns of cloud fields A, B, and C using the green vegetation surface type.

TABLE 3. Inherent and retrieved averaged cloud properties for the three cloud fields using the green vegetation surface type.

Cloud field	$\bar{\tau}_{inh}$	$\bar{\tau}_{ret}$	$\frac{\bar{\rho}_{ret} - \bar{\rho}_{inh}}{\bar{\rho}_{inh}}$	$\frac{\bar{\tau}_{ret} - \bar{\tau}_{inh}}{\bar{\tau}_{inh}}$
Scattered arctic stratocumulus (A)	4.3	4.4	4.0%	4.0%
Broken arctic stratocumulus (B)	14.0	13.1	−3.4%	−5.9%
Fair weather cumulus (C)	55.8	45.3	−4.0%	−18.8%

sharp increases in $\bar{\tau}_{ret}$. Rather, they stem from the fact that equal but opposite sign errors in the numerator of (1) serve to overestimate τ_{ret} more than underestimate it. In this case, both the effects of correlated and uncorrelated errors play a role, but because of the asymptotic dependence of τ on reflectance, uncorrelated noise will have the more destructive impact. This discussion is related much to errors addressed by BM01 regarding poor sampling of areal mean surface irradiance along the measurement transect, and errors due to estimation of surface albedos.

The plots of rmse show how much retrievals can be affected by radiance noise. This demonstrates clearly the necessity of having a surface with as large a value of $\Delta\alpha_\lambda$ as possible and precise instrumentation.

b. Sensitivity to aerosols

Thus far, atmospheres have consisted of either cloudy or clear columns with attenuation of radiation by cloud droplets only. However, aerosol particles also have an important impact on solar radiation (e.g., Charlson and Heintzenberg 1995). Atmospheric aerosols are ubiquitous but vary in time and space. In this subsection, the impact of aerosols on retrievals of τ is examined. To simplify matters, a homogeneous aerosol was added with optical depth $\tau^{aer} = 0.2$ between surface and top of model domain, single-scattering albedo $\varpi_0^{aer} = 0.9$, and asymmetry parameter $g^{aer} = 0.7$. These parameters are typical for near-source continental, nonurban aerosols (Andreae 1995).

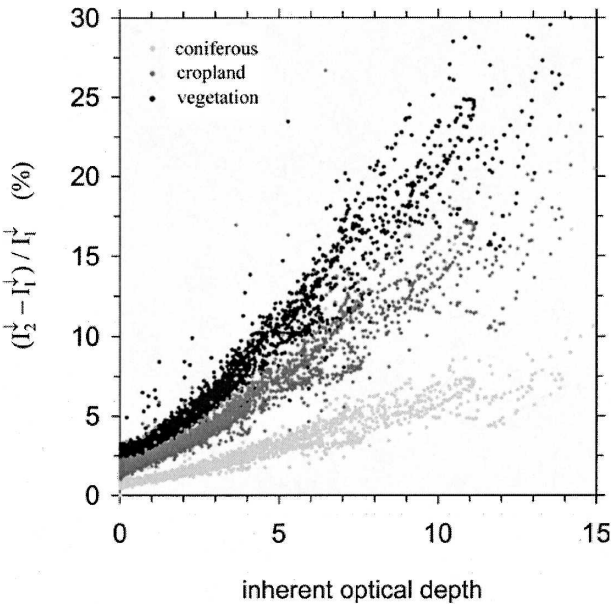

FIG. 5. Relative differences between spectral radiances as functions of inherent optical depth for cloud field A and the green vegetation, cropland, and coniferous surfaces.

Until now, it was easy to discern between clear and cloudy columns as the former did not generate radiance. When aerosols are added, this is no longer the case and a clear–cloudy threshold method must be established. This task, however, is not simple since thresholds will have to be dynamic and depend to some extent on cloud structure (through horizontal photon transport) and illumination geometry.

Figure 7 shows retrieved cloud fraction and $\bar{\tau}_{ret}$ as functions of retrieved τ threshold τ^* up to 2.5 for the three cloud fields and the green vegetation surface (use of the other surfaces produced curves of almost identical character). Here, if $\tau_{ret} < \tau^*$, τ_{ret} was reset to 0. For very small τ^*, all columns were assumed to be cloudy and so estimated cloud fraction reaches unity and $\bar{\tau}_{ret}$ is minimized. As τ^* increases, very little happens to retrieved cloud fraction and $\bar{\tau}_{ret}$. Near $\tau^* = 0.5$, however, for cloud field A, cloud fraction and $\bar{\tau}_{ret}$ catastrophically reach their correct inherent values. Note that $\tau^* = 0.5$ exceeds $\tau^{aer} = 0.2$ because retrievals are based on the assumption that only clouds are present. Hence, when aerosols occur with relatively small g, the algorithm mistakes them for a relatively thick cloud (but not as thick as it could have been had ϖ_0^{aer} been 1.0 rather than 0.9). As τ^* continues to increase, cloud fraction keeps decreasing and $\bar{\tau}_{ret}$ increasing but at a much slower, and near constant, rate due to the progressive removal of thin cloud columns.

For cloud field B, a similar pattern is observed but with some noteworthy differences. First, a larger τ^* has to be reached before the aerosol signal is surpassed. This can be explained by horizontal transport of photons out cloud sides. Larger mean τ_{inh} and cloud fraction of field B both produce stronger convergence of photons in intercloud aerosol regions. This translates into more radiance coming from aerosol columns compared to field A. Another feature is the smoother decrease in cloud fraction and increase in $\bar{\tau}_{ret}$ once the aerosol signal is surpassed. This is due to a small fraction of thin cloud τ for this scene. Finally, note that τ_{ret} remains smaller than inherent values. In this case,

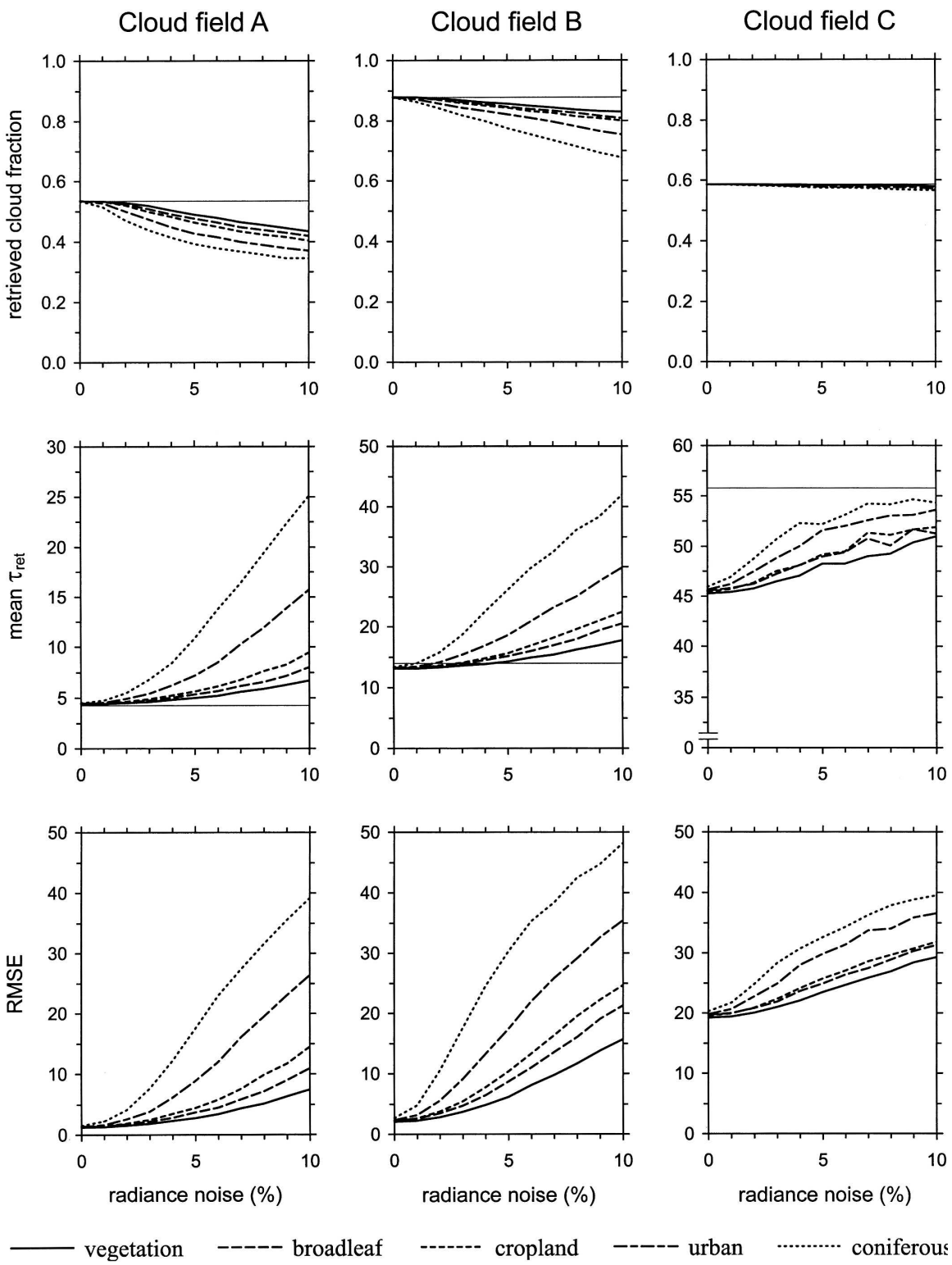

FIG. 6. Retrieved cloud fraction, $\bar{\tau}_{ret}$ and rmse as function of radiance noise for the three cloud fields. The thin continuous line represents inherent values. Results are averages over 10 independent simulations.

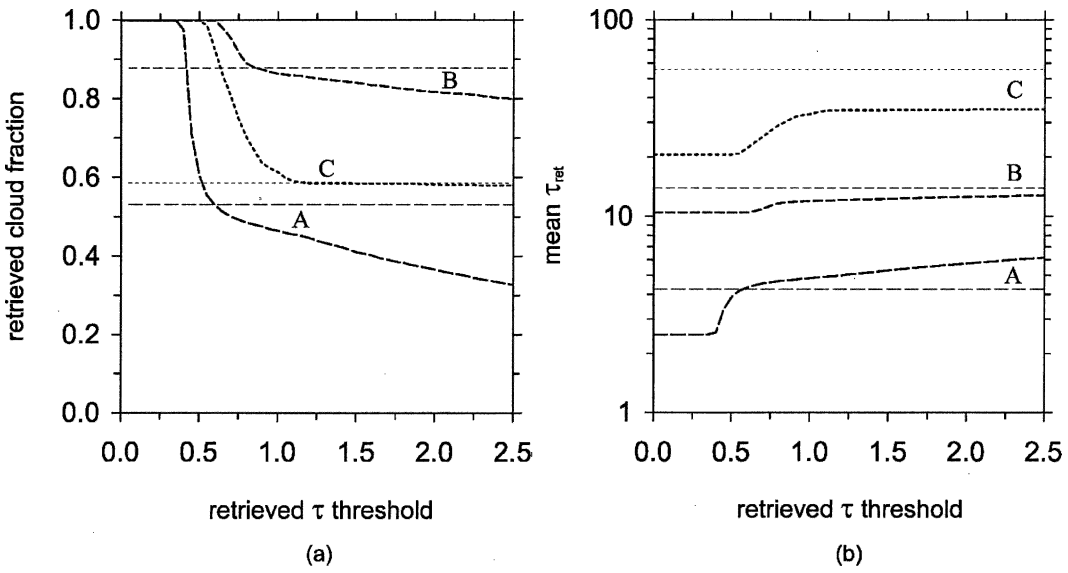

FIG. 7. (a) Retrieved cloud fraction and (b) $\bar{\tau}_{ret}$ as functions of retrieved τ threshold for cloud fields A, B, and C and the green vegetation surface type. The corresponding thin lines represent inherent values (see Table 1).

longer optical paths traversed by photons play a role: absorption by relatively large numbers of aerosol scattering events removes energy which reduces reflectance which in turn is interpreted by the retrieval algorithm as reduced τ.

For cloud field C, the quasi-absence of thin cloud columns forms a veritable plateau at large τ^*. Also, photon convergence between thick clouds explains why a value of $\tau^* \approx 1.1$ had to be achieved before aerosols were surpassed. In addition, $\bar{\tau}_{ret}$ is much underestimated for this field, an effect resulting from absorption and the loss of sensitivity for large τ.

To see more precisely how aerosols affect retrievals as a function of τ_{inh}, Fig. 8 presents an intercomparison between τ_{inh} and τ_{ret} for all three cloud fields together for a case with and without aerosols using the green vegetation surface. As expected, when aerosols are included, small τ_{inh} are highly overestimated. This prevents τ_{ret} from being lower than 0.4. For larger τ_{inh}, absorption by aerosol attenuates cloud reflectance and τ_{ret} are underestimated.

Thus, a potential method for setting τ^* when using real data might be to simply generate curves like those shown in Fig. 7 and determine at what values of τ^* the second derivatives of cloud fraction and mean τ with respect to τ^* become very close to zero. This will occur for two values of τ^*, the larger value being the one of interest. Then, repeat the retrieval using this threshold, to provide final estimates of τ_{ret}. Since the algorithm executes very quickly, repeated application to isolate τ^* is not as computationally taxing as it sounds.

5. Conclusions

The main objective of this study was to analyze the surface-based cloud optical depth retrieval algorithm developed by Barker and Marshak (2001). Its sensitivity to two key parameters that influence the accuracy of the retrievals was assessed: instrument noise and presence of aerosol.

Instrument fidelity can be a critical issue for the al-

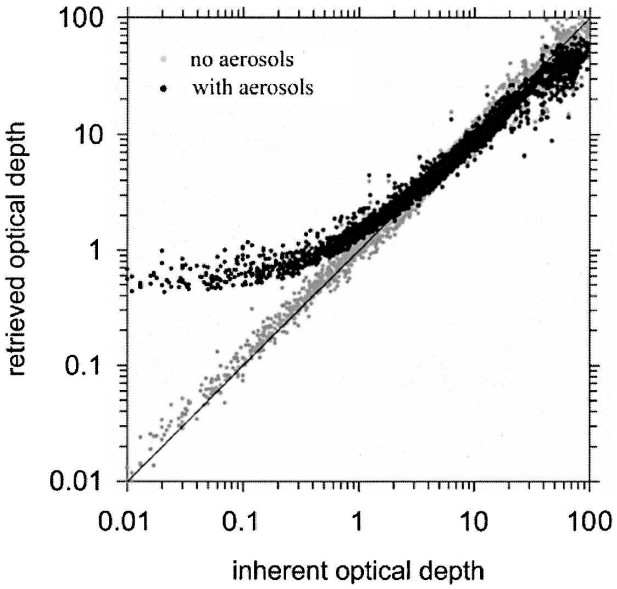

FIG. 8. Scatterplot of retrieved vs inherent optical depths for the three cloud fields together with and without aerosols.

gorithm's accuracy. Results shown take into account the precision part only and not the accuracy that affects initial calibration. Here, the issue is signal-to-noise ratio in the spectral radiance difference. For small τ_{inh}, uncorrelated noise can become so important that it totally overwhelms the signal. This can result in flagging some of the thinner cloud columns as cloudless. Conversely, noise can amplify the spectral radiance difference and in this case large values of τ_{inh} can produce apparent reflectance estimates >1. When this occurred, they were reset to 100 (the retrieval algorithm's maximum value).

When aerosol is present, as it always is, the issue is determination of optical depth threshold τ^* that will allow for optimal partition between cloudy and cloud-free columns. Results presented in Fig. 7 suggest that this segregation might be made when the second derivatives of cloud fraction and mean (and perhaps higher moments of) optical depth with respect to τ^* stabilize.

In addition to these sources of uncertainties, two other parameters were found to affect the algorithm's efficiency. These are the mean inherent τ of the cloud field and the difference in spectral surface albedo for the two observing wavelengths. The main problem with mean τ is that as it increases, cloud reflectance becomes increasingly insensitive to changes in τ. This means that errors made on retrieved reflectance by the algorithm will be more destructive for optically thick cloud fields. Finally, the difference between spectral surface albedos $\Delta\alpha_\lambda$ has a major impact on retrievals (cf. BM01). This is because division by two small terms in (1) makes results extremely sensitive to the accuracy of the measurements.

Acknowledgments. The work presented in this paper was supported in part by the Canadian Space Agency (CSA) and the Meteorological Service of Canada (MSC) through the Cloudsat program, and also from the Modelling of Clouds and Climate Proposal which is funded through the Canadian Foundation for Climate and Atmospheric Sciences, the Meteorological Service of Canada, and the Natural Sciences and Engineering Research Council. The first author received Université du Québec à Montréal (UQAM) bursaries from the Department of Earth and Atmospheric Sciences and also from the Canadian Meteorological and Oceanographic Society (CMOS) through Student Travel Bursaries. We thank W. Szyrmer, A. Trishchenko, and N. O'Neill for their support in various part of the work, and are grateful to C. Pavloski and A. Marshak for helpful discussions. We also acknowledge the help of UQAM Department of Physics and the Center for Research in Geochemistry and Geodynamics (GEOTOP) for making computer time available.

REFERENCES

Andreae, M. O., 1995: Climatic effects of changing atmospheric aerosol levels. *World Survey of Climatology,* Vol. 16, *Future Climates of the World,* A. Henderson-Sellers, Ed., Elsevier, 341–392.

Barker, H. W., 1991: Solar radiative fluxes for realistic extended broken cloud fields above reflecting surfaces. Ph.D. thesis, McMaster University, 257 pp.

——, and D. Liu, 1995: Inferring optical depth of broken clouds from Landsat data. *J. Climate,* **8,** 2620–2630.

——, and A. Marshak, 2001: Inferring optical depth of broken clouds above green vegetation using surface solar radiometric measurements. *J. Atmos. Sci.,* **58,** 2989–3006.

——, T. J. Curtis, E. Leontieva, and K. Stamnes, 1998: Optical depth of overcast cloud across Canada: Estimates based on surface pyranometer and satellite measurements. *J. Climate,* **11,** 2980–2994.

——, A. Marshak, W. Szyrmer, A. P. Trishchenko, J.-P. Blanchet, and Z. Li, 2002: Inference of cloud optical depth from aircraft-based solar radiometric measurements. *J. Atmos. Sci.,* **59,** 2093–2111.

Boers, R., 1997: Simultaneous retrievals of cloud optical depth and droplet concentration from solar irradiance and microwave liquid water cloud. *J. Geophys. Res.,* **102,** 29 881–29 891.

——, A. Van Lammeren, and A. Feijt, 2000: Accuracy of cloud optical depth retrievals from ground-based pyranometers. *J. Atmos. Oceanic Technol.,* **17,** 916–927.

Brenguier, J.-L., 1991: Parameterization of the condensation process: A theoretical approach. *J. Atmos. Sci.,* **48,** 264–282.

——, and W. W. Grabowski, 1993: Cumulus entrainment and cloud droplet spectra: A numerical model within a two-dimensional dynamical framework. *J. Atmos. Sci.,* **50,** 120–136.

Caya, D., and R. Laprise, 1999: A semi-implicit semi-Lagrangian Regional Climate Model: The Canadian RCM. *Mon. Wea. Rev.,* **127,** 341–362.

Charlson, R. J., and J. Heintzenberg, Eds., 1995: *Aerosol Forcing of Climate*. John Wiley and Sons, 416 pp.

Cihlar, J., J. Beaubien, R. Latifovic, and G. Simard, 1999: Land Cover of Canada Version 1.1. Special Publication, NBIOME Project, Canada Centre for Remote Sensing and the Canadian Forest Service, Natural Resources Canada, CD-ROM.

Henyey, L. C., and J. L. Greenstein, 1941: Diffuse radiation in the galaxy. *Astrophys. J.,* **93,** 70–83.

Leontieva, E., K. Stamnes, and Y. A. Olseth, 1994: Cloud optical properties at Bergen (Norway) based on the analysis of long-term solar irradiance records. *Theor. Appl. Climatol.,* **50,** 73–82.

Leontyeva, E., and K. Stamnes, 1994: Estimations of cloud optical thickness from ground-based measurements of incoming solar radiation in the Arctic. *J. Climate,* **7,** 566–578.

Loeb, N. G., and R. Davies, 1996: Observational evidence of plane parallel model biases: The apparent dependence of

cloud optical depth on solar zenith angle. *J. Geophys. Res.,* **101,** 1621–1634.

——, and J. A. Coakley Jr., 1998: Inference of marine stratus cloud optical depths from satellite measurements: Does 1D theory apply? *J. Climate,* **11,** 215–232.

Marchuk, G. I., G. A. Mikhailov, M. A. Nazoraliev, R. A. Dorbinjin, B. A. Kargin, and B. S. Elepov, 1980: *Monte Carlo Methods in Atmospheric Optics.* Series in Optical Science, Vol. 12, Springer-Verlag, 208 pp.

Marshak, A., A. B. Davis, W. J. Wiscombe, and R. Calahan, 1995: Radiative smoothing in fractal clouds. *J. Geophys. Res.,* **100,** 26 247–26 261.

——, Y. Knyazikhan, A. B. Davis, W. J. Wiscombe, and P. Pilewskie, 2000: Cloud-vegetation interaction: Use of normalized difference cloud index for estimation of cloud optical thickness. *Geophys. Res. Lett.,* **27,** 1695–1698.

Park, P. S., and Coauthors, 2000: Study on synergetic observations of Earth Radiation Mission Instruments. ESTEC Contract 12068/96/NL/CN, Final Report, 281 pp.

Rossow, W. B., and R. A. Schiffer, 1991: ISCCP cloud data products. *Bull. Amer. Meteor. Soc.,* **72,** 2–20.

Stamnes, K., S.-C. Tsay, W. Wiscombe, and K. Jayaweera, 1988: Numerically stable algorithm for discrete-ordinate-method radiative transfer in multiple scattering and emitting layered media. *Appl. Opt.,* **27,** 2502–2509.

Szyrmer, W., 1998: Étude des processus microphysiques dans l'atmosphère à l'aide d'un modèle numérique. Ph.D. thesis, Université du Québec à Montréal, Montréal, Québec, Canada, 340 pp.

——, and I. Zawadzki, 1999: Modeling of the melting layer. Part I: Dynamics and microphysics. *J. Atmos. Sci.,* **56,** 3573–3592.